materials

MDPI

Article

The Impact of Microwave Annealing on MoS_2 Devices Assisted by Neural Network-Based Big Data Analysis

Xing Su [1,2,†], Siwei Cui [1,2,†], Yifei Zhang [1,2], Hui Yang [3,4,*] and Dongping Wu [1,2,*]

[1] State Key Laboratory of ASIC and System, Fudan University, Shanghai 200433, China; 20112020025@fudan.edu.cn (X.S.); 18112020003@fudan.edu.cn (S.C.); 19112020021@fudan.edu.cn (Y.Z.)
[2] School of Microelectronics, Fudan University, Shanghai 200433, China
[3] School of Artificial Intelligence Science and Technology, University of Shanghai for Science and Technology, Shanghai 200093, China
[4] Institute of Photonic Chips, University of Shanghai for Science and Technology, Shanghai 200093, China
* Correspondence: yanghui_2022@usst.edu.cn (H.Y.); dongpingwu@fudan.edu.cn (D.W.)
† These authors contributed equally to this work.

Abstract: Microwave annealing, an emerging annealing method known for its efficiency and low thermal budget, has established a foundational research base in the annealing of molybdenum disulfide (MoS_2) devices. Typically, to obtain high-quality MoS_2 devices, mechanical exfoliation is commonly employed. This method's challenge lies in achieving uniform film thickness, which limits the use of extensive data for studying the effects of microwave annealing on the MoS_2 devices. In this experiment, we utilized a neural network approach based on the HSV (hue, saturation, value) color space to assist in distinguishing film thickness for the fabrication of numerous MoS_2 devices with enhanced uniformity and consistency. This method allowed us to precisely assess the impact of microwave annealing on device performance. We discovered a relationship between the device's electrical performance and the annealing power. By analyzing the statistical data of these electrical parameters, we identified the optimal annealing power for MoS_2 devices as 700 W, providing insights and guidance for the microwave annealing process of two-dimensional materials.

Keywords: microwave annealing; molybdenum disulfide devices; two dimensional materials; neural network; HSV color

check for updates

Citation: Su, X.; Cui, S.; Zhang, Y.; Yang, H.; Wu, D. The Impact of Microwave Annealing on MoS_2 Devices Assisted by Neural Network-Based Big Data Analysis. *Materials* **2024**, *17*, 3373. https://doi.org/10.3390/ma17133373

Academic Editor: Marek Sierka

Received: 18 May 2024
Revised: 3 July 2024
Accepted: 5 July 2024
Published: 8 July 2024

Copyright: © 2024 by the authors. Licensee MDPI, Basel, Switzerland. This article is an open access article distributed under the terms and conditions of the Creative Commons Attribution (CC BY) license (https://creativecommons.org/licenses/by/4.0/).

1. Introduction

Over the past decade, research endeavors have yielded significant advancements in the domain of two-dimensional (2D) materials. These materials, characterized by their layered structure, exhibit remarkable and industrially relevant properties when reduced to a thickness of just a few atomic layers. Molybdenum disulfide (MoS_2), a quintessential example of 2D materials, has garnered considerable attention for its superior mechanical, optical, and electrical properties [1]. Notably, MoS_2 is distinguished by its energy bandgap, which ranges between 1.2 and 1.8 eV, offering a distinct advantage over graphene, which lacks an intrinsic bandgap. This characteristic endows MoS_2 with great potential for application in field-effect transistors (FETs) and other electronic devices.

The Schottky barrier [2] refers to a rectifying barrier formed at the metal–semiconductor interface, characterized by a lower interface voltage and a relatively thin depletion layer at the metal end, affecting current flow and posing an obstacle to device performance. These device performances generally refer to the on/off current, mobility, contact resistance, and subthreshold slope of the device. The Schottky barrier between metal and MoS_2 presents a significant obstacle to device performance [3], exacerbated by MoS_2's propensity to adsorb airborne contaminants due to its two-dimensional nature [4]. This interaction not only compromises device integrity but also hinders its operational efficiency. To mitigate the impact of the metal–MoS_2 barrier, various strategies have been devised, such as implementing

highly doped semiconductor contacts [5] and employing scandium electrodes [6]. However, these solutions face their own sets of challenges: the instability of highly doped contacts and the complexity and cost associated with scandium electrodes limit their industrial applicability. In contrast, annealing techniques have emerged as a widely adopted solution for removing adsorbed impurities from thin film [7]; during annealing, metal atoms are capable of diffusing to the surface or interface region of the semiconductor, filling interface defects. This mechanism enhances the adhesion between the metal and semiconductor, minimizes the density of interface states, and subsequently lowers the contact resistance [8]. Thermal annealing can also reduce these interface defects and states, enhancing carrier transport at the interface [9]. Furthermore, it triggers phase transformations or chemical reactions in the interface region, forming new phases or compounds with lower contact resistance [10]. Techniques such as rapid thermal annealing [11], high-vacuum annealing [12], and laser annealing [8] have been extensively utilized for this purpose, offering a more practical approach to enhancing device performance and longevity.

However, the annealing methods commonly employed are not compatible with flexible MoS_2 devices, as the typical annealing temperatures exceed 150 °C [13,14]. Such high temperatures can easily damage flexible devices and require prolonged processing times, often exceeding 30 min. Although laser annealing offers the advantage of selective heating, its efficiency is notably low. Moreover, the equipment necessary for laser annealing is costly, rendering it impractical for uniform annealing of devices in large batches. Microwave annealing (MWA), a novel technique emerging in recent years, offers the advantage of a low thermal budget. This method facilitates a reduction in contact resistance for devices and aids in the removal of contaminants adsorbed onto the MoS_2 channels [15–17]. These outcomes stem from the heat generated by electromagnetic loss between the material and the microwaves, similar to the effect of thermal annealing. However, current research on microwave annealing primarily focuses on dopant activation and the formation of ultra-shallow junctions [18], with limited investigations into its effects on MoS_2 devices.

In the current field of MWA research, the majority of experiments are conducted using limited samples, as demonstrated in studies [15,19]. These investigations have confirmed that microwave annealing has a positive effect on the performance of MoS_2 devices. However, there is a notable absence of comprehensive research based on large datasets examining the uniform effects of MWA on the performance of MoS_2 devices. This research gap primarily arises from the challenges associated with fabricating numerous devices and standardizing parameters, which present significant operational difficulties. Particularly in the production of MoS_2 devices, the inconsistency in film thickness due to the use of the mechanical exfoliation method poses a major issue.

The impact of MWA can vary drastically with differences in film thickness. Thus, ensuring uniform thickness is critical for the reliability of the research findings. CVD can grow uniform MoS_2 films on large-area substrates, which is essential for mass production and industrial applications [20]. Additionally, CVD process parameters (such as temperature, pressure, gas flow, etc.) can be precisely controlled to adjust the thickness, grain size, and morphology of the MoS_2 films [21]. Despite CVD's excellent scalability for industrial-scale production [22], the MoS_2 films produced by this method may contain more defects and grain boundaries, affecting their electronic and optical properties [23]. In contrast, MoS_2 sheets prepared by mechanical exfoliation typically exhibit higher crystal quality and lower defect density, making them suitable for research on high-performance electronic devices [24]. Currently, MoS_2 devices prepared using the mechanical exfoliation method require film thickness to be measured individually using Atomic Force Microscopy (AFM), a process that becomes particularly cumbersome when handling large batches of samples. As a result, visual inspection of film thickness during the exfoliation process is the prevalent method, though this approach relies heavily on human experience and can lead to significant variances in accuracy between individuals. Therefore, there is an urgent need to develop a new technological method to assist in the mechanical exfoliation process, enabling accurate identification and classification of film thickness, thereby improving the

accuracy of recognition while reducing experimental costs. Furthermore, clear guidance on how to effectively apply MWA to enhance the performance of MoS_2-based devices is currently lacking.

In this study, we prepared MoS_2 devices on a large scale via mechanical exfoliation. It was crucial to collect comprehensive data and maintain consistency in parameters to effectively analyze the impact of microwave annealing. To enhance the accuracy of film thickness identification and reduce the time required for device fabrication, we employed a neural network method based on the HSV color space. This approach not only improved accuracy compared to traditional visual inspection but also significantly reduced the time needed for mass fabrication, ensuring uniformity of the films throughout the experimental process. Subsequently, we subjected the devices to MWA and extracted their electrical performance parameters. Statistical analysis of these parameters allowed us to determine an optimal MWA power setting that significantly enhanced device performance, achieving maximal improvement in their electrical characteristics.

2. Experiment

2.1. Classification of MoS_2 Film Thickness

In our experiments, investigating the MWA power for research devices often necessitates the preparation of a large number of devices while ensuring uniformity in channel dimensions and film thickness. Our devices are fabricated using a mechanical exfoliation method from commercial natural MoS_2 crystals (XFNANO Inc., Nanjing, China, where the thickness of MoS_2 film under an optical microscope is typically determined by visual inspection. In the process of preparing numerous devices, this step is both tedious and prone to errors. Consequently, there is a need to identify a new method to replace the visual recognition pattern, with the aim of reducing the experimental duration and increasing the accuracy of thickness determination. Human recognition of film thickness primarily relies on the HSV color space model, whereas optical microscopes generally save images in the RGB (red, green, blue) color space model [25]. During the device fabrication process, the identification of MoS_2 thin films typically involves comparing the optical contrast between the MoS_2 and the dielectric layer to determine the film's thickness.

In this experiment, we classified the MoS_2 films as illustrated in Figure 1 and Table 1. Category 1 consists of monolayer MoS_2 with a typical thickness measured at approximately 0.65 nm. Category 2 comprises few-layer MoS_2, where the thickness generally ranges from approximately 1.3 nm to 6.5 nm. Category 3 includes multilayer MoS_2, with thickness measurements typically falling between approximately 6.5 nm and 32.5 nm. Category 4 features nearly bulk MoS_2, with a thickness exceeding approximately 32.5 nm. In this study, we chose to fabricate devices using Category 3, specifically, multilayer MoS_2 films. These films not only maintain the direct bandgap feature intrinsic to MoS_2 but are also more easily produced via mechanical exfoliation. Additionally, multilayer MoS_2 films display remarkable chemical stability and reduced sensitivity to environmental changes, making them exceptionally suitable for long-term applications.

Table 1. Statistical parameters of MoS_2 films.

	Category 1	**Category 2**	**Category 3**	**Category 4**
Thickness (nm)	≈0.65	≈1.3 to 6.5	≈6.5 to 32.5	More than 32.5

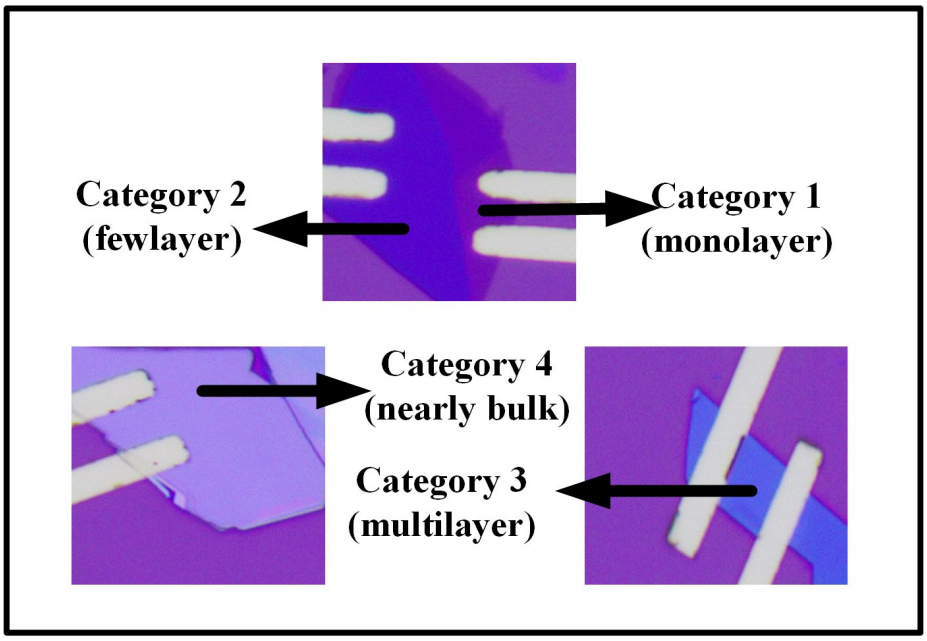


Figure 1. The classification of four typical MoS_2 thicknesses.

2.2. Advantages of Using the HSV for Film Thickness Classification

The RGB color space is characterized by an amalgamation of luminance and chromatic information, implying that variations in color within the RGB spectrum concurrently reflect changes in both brightness and hue. A substantial correlation exists among the three channels of RGB, particularly evident within image data. Figure 2 presents box-and-whisker plots for four different categories of MoS_2 film thicknesses. An examination of Figure 2 reveals that the median values of the red (R) component across all plots are closely aligned, with a similar breadth for the interquartile range, rendering the R value alone insufficient for distinguishing film thicknesses. Additionally, the boxes for the other two components, green (G) and blue (B), exhibit a certain degree of overlap across different film thicknesses. In contrast, the HSV color space aligns more closely with human perception of color by segregating hue (H), saturation (S), and value (V) into distinct components. This separation potentially facilitates a clearer expression of certain color characteristics within the HSV space, as it allows for the independent consideration of hue variations unaffected by changes in luminance. Such independence of parameters might more readily disclose color variations attributed to differences in film thickness. Figure 3 showcases box-and-whisker plots for HSV values across four categories of film thickness. The distributions of the three values are notably concentrated, particularly the hue (H), which exhibits an exceedingly narrow range of hue distribution, with lower degrees of box overlap between different film thicknesses, accentuating the distinctiveness between parameters. Conversely, while the RGB box plots display color variances, these differences may result from a complex interplay of chroma and brightness, complicating the interpretation of film thickness impact directly from the RGB plots. To simulate human recognition patterns, it is essential to convert optical images into the HSV color space [26].

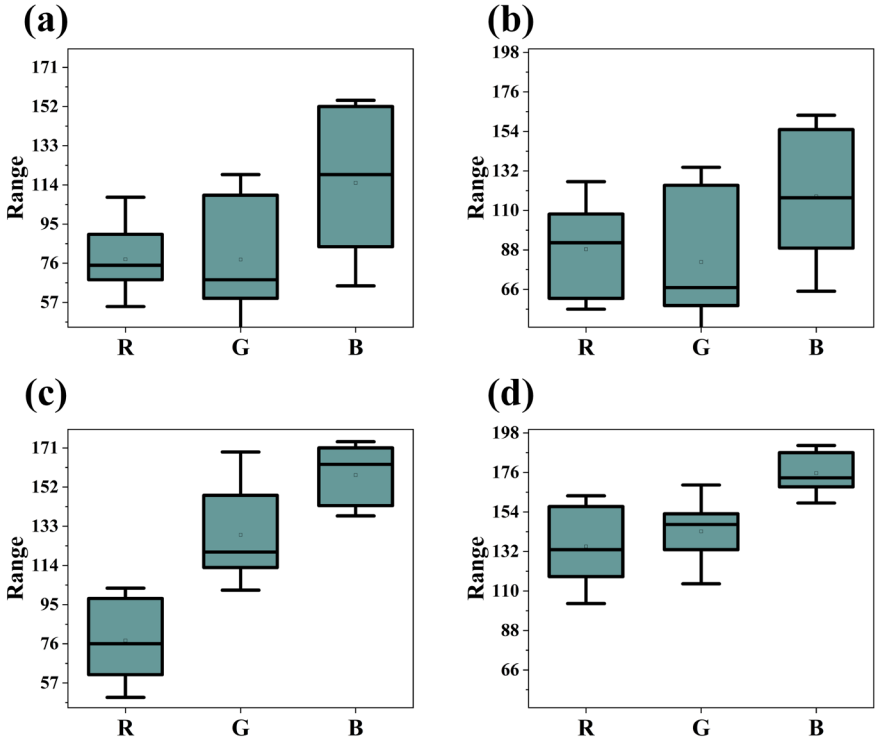


Figure 2. Box-and-whisker plots representing the distribution of RGB values across four distinct categories of film thickness: (**a**) Category 1; (**b**) Category 2; (**c**) Category 3; (**d**) Category 4.

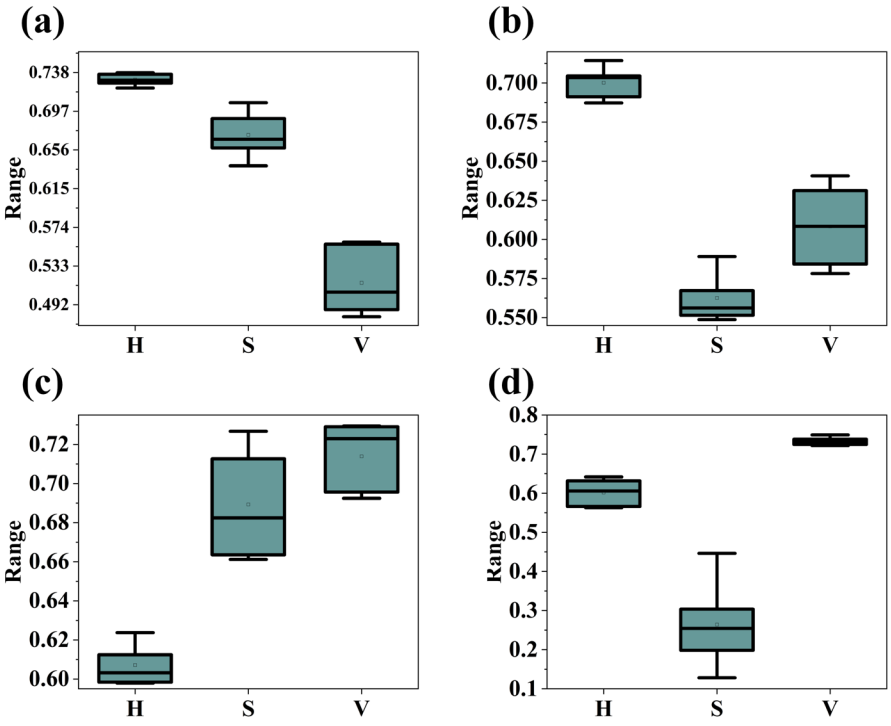


Figure 3. Box-and-whisker plots representing the distribution of HSV values across four distinct categories of film thickness: (**a**) Category 1; (**b**) Category 2; (**c**) Category 3; (**d**) Category 4.

2.3. Neural Network Based on HSV Color Space

The second step involves simulating the method by which the human eye discerns film thickness, specifically by comparing the contrast of the film on the substrate to determine the thickness. In this process, we opt to employ a neural network to implement this discrimination method. The structure of the neural network is depicted in Figure 4.

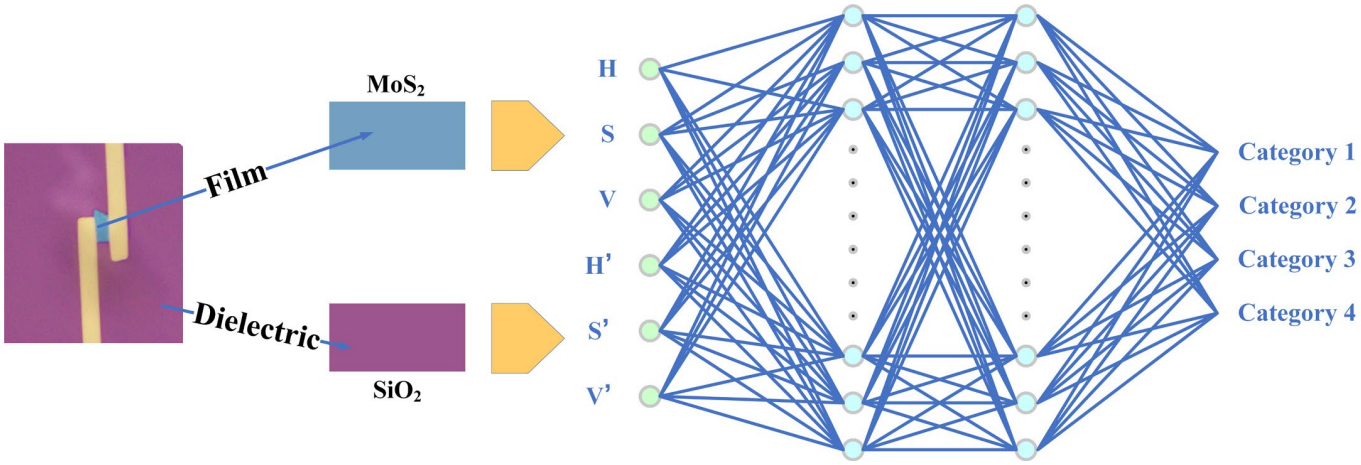


Figure 4. Neural network structure for discriminating membrane thickness.

As illustrated in Figure 4, the neural network utilized in this study takes six inputs, which comprise three values from the HSV color space of MoS_2 thin films and three values from the HSV color space of the silicon dioxide (SiO_2) dielectric layer adjacent to the films. The neural network features two hidden layers: the first hidden layer contains 128 nodes and employs the Rectified Linear Unit (ReLU) [27] activation function to ensure nonlinear learning capability. The second hidden layer has its number of nodes halved to 64, also utilizing the ReLU activation function. Given the Adam optimizer's effective performance on such problems [28,29], it was selected as the optimizer for this network, with a learning rate set at 0.001. The dataset was divided, allocating 80% for training and the remaining 20% for validation; the neural network in this article is based on PyTorch of python (The version of Python is 3.11.5).

2.4. Classification Results

Figure 5a illustrates the curve depicting how the neural network's loss on the validation set changes with epochs. From the figure, it is evident that the loss decreases progressively with an increasing number of training epochs, indicating a positive training trend. Figure 5b presents the confusion matrix of the prediction results. Within the confusion matrix, most predictions are concentrated along the diagonal, signifying that the model accurately classifies the majority of the samples. High values on the diagonal and low values of the diagonal demonstrate the model's strong performance across all categories, indicating excellent predictive outcomes of the network. This approach significantly reduces the time required for device fabrication compared to manual thickness identification by the human eye while also achieving high accuracy.

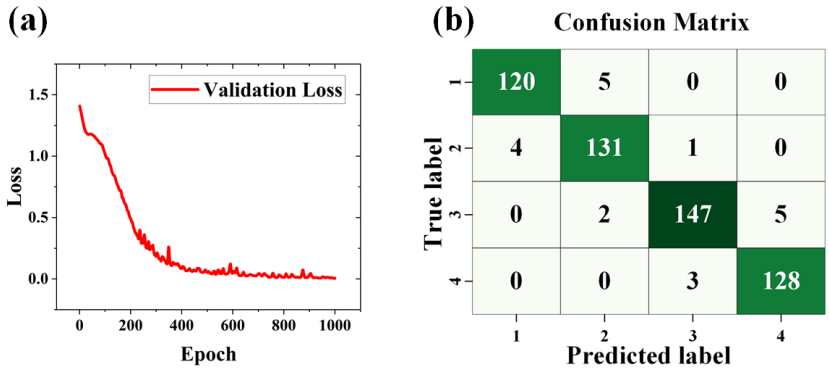


Figure 5. Showcased the training process and results of the neural network: (**a**) A graph depicting the change in validation loss over epochs. (**b**) The confusion matrix of prediction results; 1, 2, 3, and 4 indicate Category 1, Category 2, Category 3, and Category 4.

2.5. Device Fabrication and MWA

The fabrication of multilayer MoS_2 transistors begins with the preparation of designated substrates. This involves utilizing heavily doped p-type silicon wafers, which are covered with thermally oxidized SiO_2 dielectric layers (the thickness is 230 nm). These wafers are then segmented into 1 cm × 1 cm squares, each marked for identification. Few-layer MoS_2 samples are procured via mechanical exfoliation and are subsequently transferred onto these marked squares. Prior to this transfer, the squares are meticulously cleaned using acetone, alcohol, and deionized water to ensure a contaminant-free surface. Under microscopic observation, the positions of the multilayer MoS_2 samples on the squares are accurately determined. The construction of multilayer MoS_2 transistors on these substrates is achieved through a sequence of processes, including electron beam lithography (the electron beam lithography machine used in this experiment is the JBX-6300FS, JEOL, Tokyo, Japan), physical vapor evaporation (the physical vapor deposition machine used in this experiment is the PVD 75, Kurt J. Lesker, Shanghai, China, and lift-off techniques. Chromium/gold (Cr/Au) electrodes, with thicknesses of 20/96 nm, respectively, are employed as the source–drain electrodes. To enhance device performance, MWA is applied using the AXOM-300 MWA system from DSG Company (San Jose, CA, USA). This system operates at a microwave magnetron frequency of 5.8 GHz.

Subsequently, MWA was conducted in a nitrogen atmosphere using varying microwave power levels (210 W, 490 W, 700 W, and 980 W) over a period of 600 s. Electrical evaluations were performed before and after MWA using an Agilent B1500A semiconductor characterization system (Agilent Technologies, Shanghai, China) situated within a shielded probe station at room temperature. Following the annealing process, post-annealing assessments were carried out once the device had returned to ambient temperature.

In our experiment, to ensure the consistency and reliability of the experimental data, we endeavored to maintain uniformity in both the thickness of mechanically exfoliated MoS_2 films and the dimensions of the channels across all devices. The method to achieve uniform film thickness involves utilizing neural networks to determine the thickness, a process that has been detailed extensively in prior discussions. Attaining uniformity in channel dimensions is relatively straightforward, which is accomplished by replicating the same pattern during electron beam lithography. The statistical data pertaining to the film thickness and channel dimensions of MoS_2 devices are presented in Table 2.

Table 2. Statistical parameters of MoS_2 devices.

The Mean of Film Thickness (nm)	The Variance of Film Thickness (nm^2)	Channel Length (μm)	Channel Width (μm)
7.9	0.11	3.3 ± 0.2	3.8 ± 0.2

3. Results and Discussion

Table 3 presents the temperature variations observed during various MWA procedures, as measured by an infrared thermometer positioned underneath the equipment. Within a nitrogen atmosphere, the recorded peak temperatures corresponding to microwave powers of 210 W, 490 W, 700 W, and 980 W are 60.1 °C, 87.5 °C, 121.2 °C, and 148.8 °C, respectively. From Table 3, it is evident that the peak temperatures achieved during our MWA process are consistently lower than the glass transition temperatures commonly associated with flexible semiconductor substrates, such as polyimide (PI) and polyethylene naphtholate (PEN).

Table 3. Peak temperature corresponding to different MWA power.

MWA Power	210 W	490 W	700 W	980 W
Temperature	60.1 °C	87.5 °C	121.2 °C	148.8 °C

To evaluate the impact of MWA at varying power levels on the performance of MoS_2 transistors, we performed experiments to examine the transfer characteristics of multilayer MoS_2 transistors as influenced by the annealing power. As illustrated in Figure 6, Figure 6a presents an optical photograph of a typical MoS_2 device, accompanied by precise thickness measurements obtained through AFM; the exact value of its film thickness is 7.9 nm. Figure 6b displays Raman spectroscopy characterizations of the device before and after annealing, with the black line representing pre-annealing and the red line post-annealing. From the Raman spectroscopy characterization, we can observe that the peak positions for E^1_{2g} and A_{1g} are at 382.6 cm^{-1} and 408.4 cm^{-1}, respectively, with a difference of 25.8 cm^{-1}. This difference characterizes the features of multilayer MoS_2 film. Additionally, a lower peak position at 1122.5 cm^{-1} signifies the peak corresponding to silicon (Si). From the Raman spectroscopy analysis conducted before and after annealing, it is observable that there are virtually no changes in the peak values. This comparison suggests that MWA in a nitrogen atmosphere has a minimal impact on the structural integrity of the multilayer MoS_2 film, as demonstrated by the negligible differences in the Raman spectra pre- and post-annealing [30].

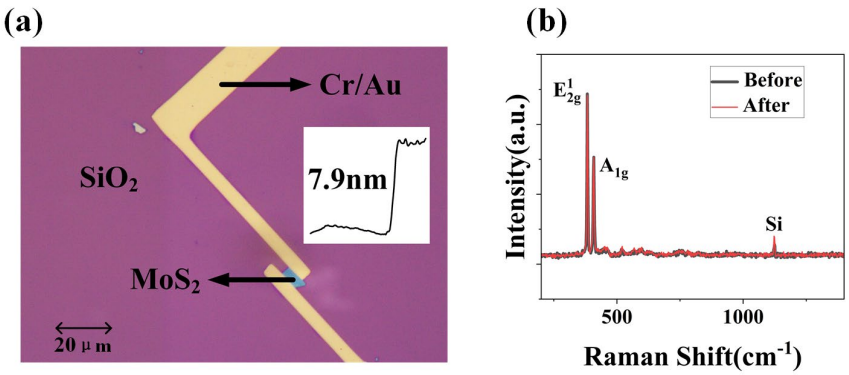


Figure 6. (**a**) Optical photograph of a typical MoS_2 device, accompanied by precise values measured via AFM before (in black) and after (in red). The scale bar in the figure is 20 μm. (**b**) Raman spectroscopy profiles before (in black) and after (in red) 700 W MWA power.

3.1. Results of Transfer and Output Characteristic Curves

Figures 7 and 8 present the transfer characteristic curves and output characteristic curves of typical multilayer MoS_2 transistors under four different annealing power settings. The transfer characteristic curves clearly demonstrate n-type behavior in the channels of the fabricated multilayer MoS_2 transistors, indicating that the drain current increases with the rise in gate voltage. Figure 7 presents schematic diagrams of the typical transfer characteristics of MoS_2 at varying power levels in our dataset. From the transfer characteristic curves

shown in Figure 7a,b, we observe an increase in the on-state current from 5.23×10^{-7} A to 5.98×10^{-7} A, a 14% improvement, under 210 W annealing power. Similarly, at a power level of 490 W, shown in Figure 7c,d, the on-state current increased from 2.06×10^{-7} A to 3.52×10^{-7} A, marking a 71% improvement. The enhancement is even more pronounced at 700 W power, where the on-state current escalated from 3.46×10^{-7} A to 9.61×10^{-7} A, an increase of 178% in Figure 7e,f. Although at 980 W power, the on-state current rose from 1.89×10^{-8} A to 5.03×10^{-8} A, a 166% increase, the improvement is still substantial in Figure 7g,h.

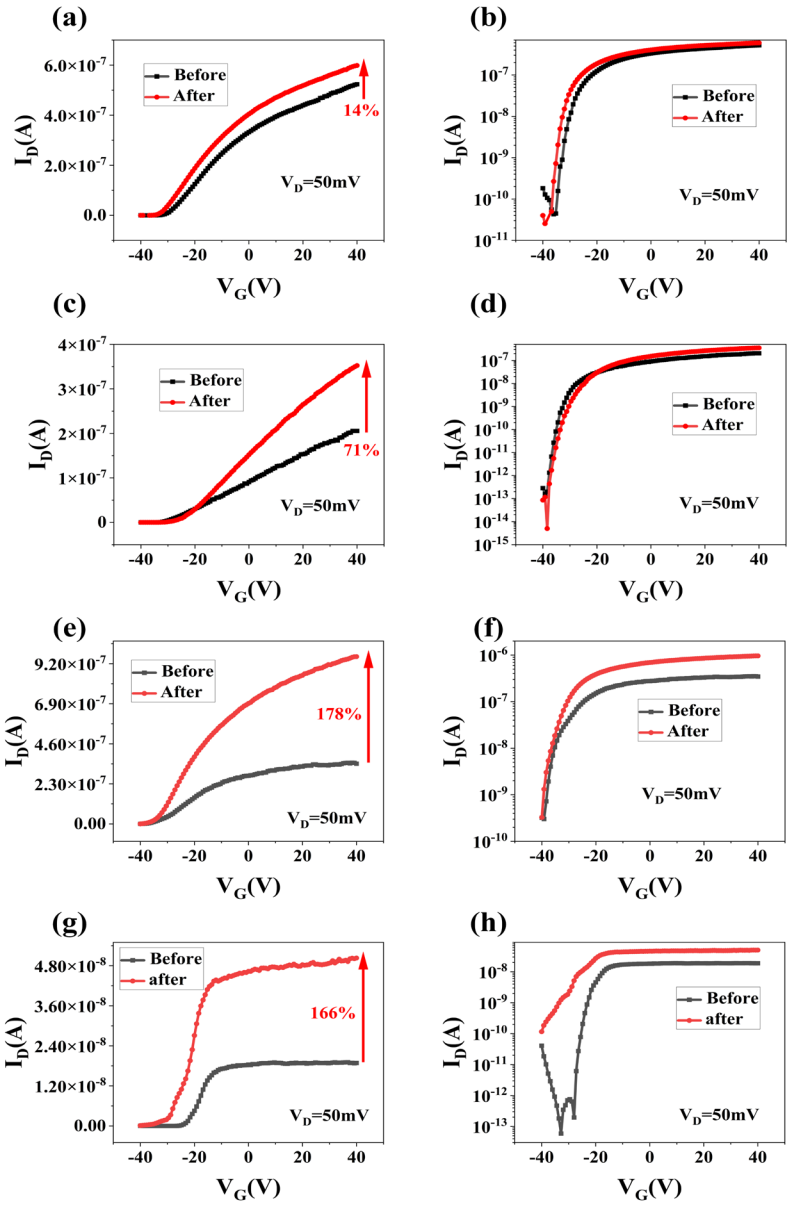


Figure 7. (**a**,**b**), respectively, depict the transfer characteristic curve and the logarithmic form of the representative MoS_2 FET following exposure to 210 W MWA power in an N_2 atmosphere. (**c**,**d**), respectively, depict the transfer characteristic curve and the logarithmic form of the representative MoS_2 FET following exposure to 490 W MWA power in an N_2 atmosphere. (**e**,**f**), respectively, depict the transfer characteristic curve and the logarithmic form of the representative MoS_2 FET following exposure to 700 W MWA power in an N_2 atmosphere. (**g**,**h**), respectively, depict the transfer characteristic curve and the logarithmic form of the representative MoS_2 FET following exposure to 980 W MWA power in an N_2 atmosphere.

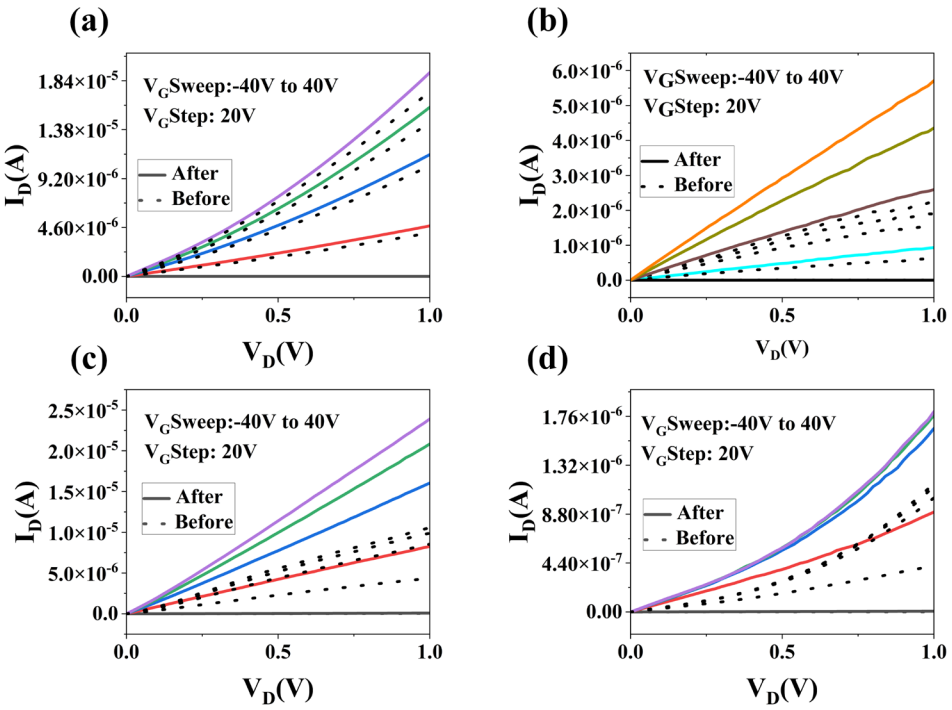


Figure 8. The curve before annealing is represented by a dotted line, and the curve after annealing is represented by a solid line. (**a**) The output curve of the representative MoS_2 FET after the 210 W MWA powers in the N_2 atmosphere. (**b**) The output curve of the representative MoS_2 FET after the 490 W MWA powers in the N_2 atmosphere. (**c**) The output curve of the representative MoS_2 FET after the 700 W MWA powers in the N_2 atmosphere. (**d**) The output curve of the representative MoS_2 FET after the 980 W MWA powers in the N_2 atmosphere.

However, it is important to note that the off-state current also experienced a significant rise at this level. The off-state current increased from 1.95×10^{-13} A to 1.16×10^{-10} A, leading to a severe degradation in the on/off ratio; the on/off ratio is only 4.34×10^{2} after microwave annealing. From the transfer characteristic curves of MoS_2 devices, it is evident that MWA has a significant positive correlation with the device's on-state current. This means that as the annealing power increases, the on-state current also gradually increases. However, an increase in annealing power is not always beneficial. Specifically, when the annealing power exceeds 700 W, there is a noticeable increase in the off-state current, which is disadvantageous for achieving an ideal on/off ratio in the device.

Figure 8 illustrates the output characteristic curves of MoS_2 devices before and after MWA at various power levels. It is evident from the figure that, under the same gate voltage, the source–drain current increases post-annealing compared to its pre-annealed state, with the most significant enhancements observed following annealing at 700 W and 980 W microwave power. This observation is consistent with the analysis of the transfer characteristic curves presented in Figure 8, underscoring the pronounced effect of MWA on enhancing the on-state current.

3.2. Results of Other Electrical Parameters

Additionally, we evaluated the average of the normalized on-state current across four few-layer MoS_2 transistors subjected to annealing in an N_2 atmosphere as a function of the annealing power, depicted in Figure 9a. The on-state current is identified as the maximal output current achieved within a high gate voltage range. The reference point for normalizing the on-state current is its value for the corresponding multilayer MoS_2 transistor prior to annealing. It is evident that the on-state current of MoS_2 devices increases with escalating annealing power, indicating a positive correlation between MWA and the on-state current of the devices. Subsequently, we investigated the relationship

between the subthreshold swing (SS), defined as $SS = \frac{dV_g}{d(\log_{10} I_d)}$, and the annealing power. Figure 9b showcases statistical data across various microwave powers, and it reveals that the subthreshold swing decreases with increasing annealing power; however, a notable increase in the subthreshold swing is observed when the annealing power exceeds 700 W, indicating a deterioration in device performance at excessively high annealing powers.

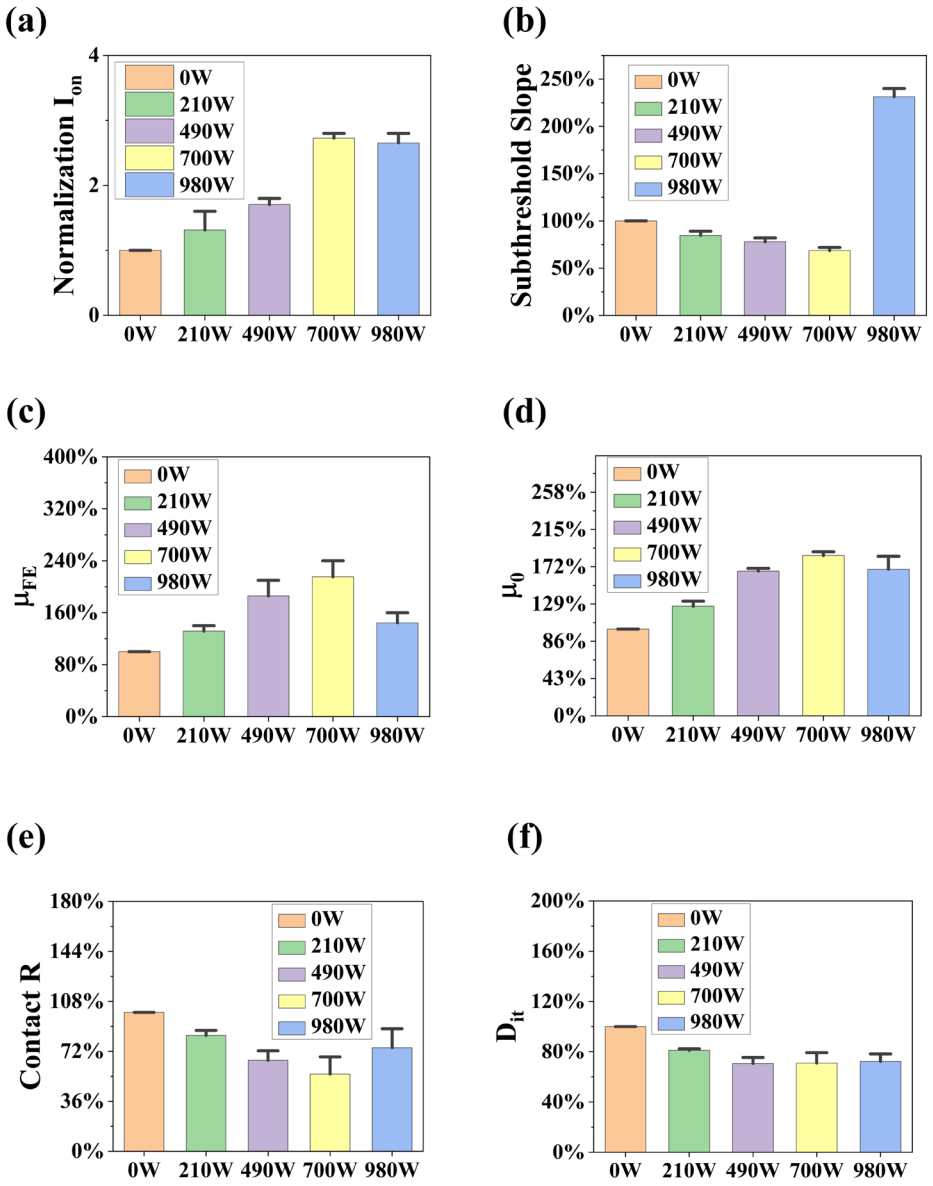


Figure 9. (**a**) Statistical data on the on-state current. (**b**) Statistical data on the subthreshold slope. (**c**) Statistical data on the field-effect mobility. (**d**) Statistical data on the intrinsic mobility. (**e**) Statistical data on the contact resistance. (**f**) Statistical data on the trap density.

Further investigations were conducted on the variation in field-effect and intrinsic mobility with annealing power; field-effect mobility is a critical parameter for assessing the performance of MOSFETs. A high field-effect mobility indicates that the MOSFET possesses superior switching speeds and lower power consumption. The field-effect mobility can be calculated using the following equation [16,31]:

$$\mu_{eff} = \frac{Lg_m}{WC_{ox}V_{DS}} \quad (1)$$

Compared to field-effect mobility, intrinsic mobility values are not influenced by contact resistance. Consequently, intrinsic mobility can be utilized to determine whether the MWA effects on MoS_2 transistors occur at the metal–semiconductor interface or within the MoS_2 channel itself. The value of intrinsic mobility can be calculated using the Y-function formula described in the literature [8]:

$$Y = \frac{I_{ds}}{\sqrt{g_m}} = \sqrt{\frac{W}{L}\mu_0 C_{ox} V_{ds}} \cdot (V_{gs} - V_{th}) \quad (2)$$

Figure 9c,d display the statistical distribution of field-effect mobility and intrinsic mobility data. It can be observed that the field-effect mobility gradually increases with the rise in annealing power until it reaches 700 W, beyond which it begins to decline. The trend in intrinsic mobility mirrors that of field-effect mobility, albeit with a relatively lower rate of increase. This indicates that the impact of MWA on the metal–semiconductor contact area is significantly greater than its effect on the MoS_2 channel. There are two main reasons for this. Firstly, MoS_2 is a material with low electromagnetic loss. Thus, it does not generate heat through electromagnetic losses in a microwave field; its temperature primarily relies on thermal conduction. Secondly, the MoS_2 thin films in our experiment were prepared using a mechanical exfoliation technique, ensuring high film quality from the start. The annealing process primarily serves to remove contaminants adsorbed due to the two-dimensional nature of the material.

To further analyze the impact of MWA on device performance, we extracted trends in contact resistance and trap density as functions of annealing power. Figure 9e,f display the statistical data of contact resistance and trap density variations with annealing power, respectively. The generation of contact resistance primarily arises from the interaction between metals and n-type semiconductors. This is due to the work function of metals often being lower than that of semiconductors, leading to a flow of electrons from the semiconductor to the metal to balance the Fermi levels. This process results in the formation of a depletion zone at the semiconductor surface where electron concentration is diminished, subsequently creating an energy barrier known as the Schottky barrier. In the off and on states of MoS_2 transistors, thermionic emission and tunneling through the Schottky barrier, respectively, restrict charge injection. As observed in Figure 9e, the contact resistance initially shows a decreasing trend with increasing microwave power until it surpasses 700 W, after which it begins to increase. This pattern aligns with our previous analysis of mobility changes, further validating the accuracy of the annealing trend. According to the output characteristics curve and statistical data on contact resistance, the reduction in contact resistance is primarily attributed to MWA potentially increasing the carrier concentration at the interface, thereby reducing the width of the tunneling barrier. The explanation for this phenomenon is discussed in [8], mainly attributed to the post-annealing diffusion of Cr into MoS_2, forming a Cr-MoS_2 solid solution. The doped MoS_2 becomes more conductive as a result. The reduction in the tunnel barrier width by forming such solid solutions at the interface is the primary mechanism behind the decrease in contact resistance following microwave annealing. When microwave power exceeds 700 W, an increase in contact resistance is observed, potentially due to the high microwave power causing temperature increases that damage the metal–semiconductor interface. Although the measured temperatures are not high, the unique loss mechanism of microwaves in a 5.8 GHz electromagnetic environment leads to the metal electrodes, which are thinner than the skin depth, becoming efficient microwave absorbers [16]. As the microwave power gradually increases, the electrode temperature may exceed the tolerance temperature of MoS_2, thereby damaging the metal–semiconductor interface. The formula for calculating trap density is derived from the literature [17], and the results shown in Figure 9f, we observed that variations in trap density across different microwave power settings were not significant; a modest decrease in trap density was noted as the annealing power increased. Since the variation in trap density was not significantly evident, and considering the substantial correlation between trap density and the interface of the dielectric layer with the

MoS_2 film, we further characterized the dielectric layer before and after annealing (700 W) to investigate the differences in the surface of SiO_2 dielectric layer pre- and post-annealing.

3.3. AFM Results of the SiO_2 Dielectric

Figure 10 presents the AFM images of a typical SiO_2 dielectric layer before and after annealing. From the AFM images, it can be observed that the roughness average (Ra) value decreased from 0.795 nm before annealing to 0.483 nm afterward, and the root mean square (Rq) value dropped from 0.553 nm to 0.361 nm post-annealing. This suggests a minor improvement in the surface quality of the SiO_2 dielectric layer due to annealing, although the changes are almost negligible. This phenomenon is understandable, given that silicon dioxide is not an effective microwave-absorbing material. Therefore, it does not generate heat from electromagnetic loss in a microwave field. Only the thermal conduction at the metal–semiconductor junction has a certain impact on the nearby SiO_2 substrate layer. We hypothesize that the significant enhancement observed in the SiO_2 dielectric layer following MWA is primarily attributable to the elimination of impurities. These impurities, predominantly residues such as adhesives from mechanical exfoliation, are effectively removed during the process. Additionally, the procedure also eliminates water molecules adsorbed on the surface of MoS_2 [30]. Consequently, the impact of MWA on trap density is also extremely limited.

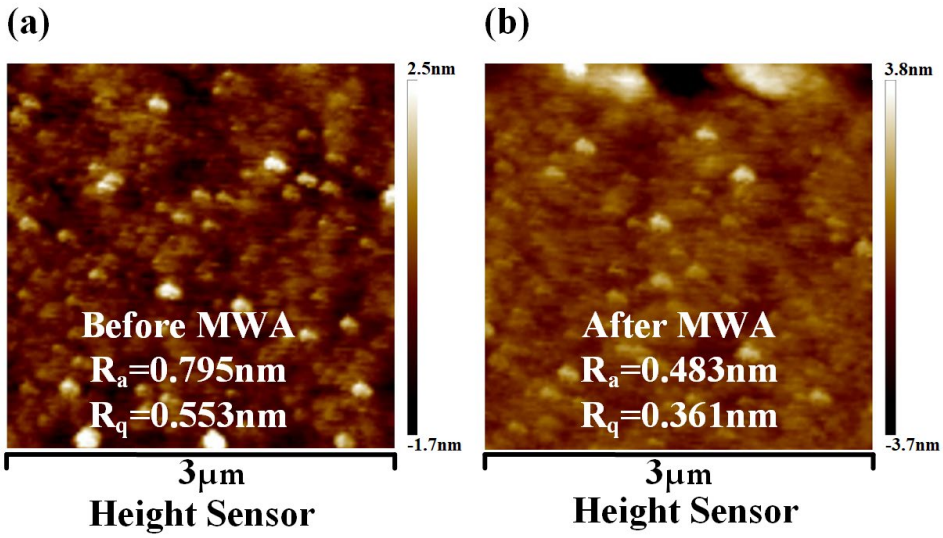


Figure 10. (**a**) AFM characterization of SiO_2 dielectric without MWA. (**b**) AFM characterization of SiO_2 dielectric after MWA at 700 W.

4. Conclusions

In this experiment, we introduced a neural network approach based on the HSV color space inspired by human methods of recognizing the thickness of MoS_2 films. This technique significantly enhances the accuracy of thickness identification during the mechanical exfoliation of large batches of devices, improving experimental efficiency and reducing the difficulty of generating extensive datasets. This method supports a comprehensive statistical analysis of the impact of MWA on the performance of MoS_2 devices. We conducted a comparative analysis of data before and after annealing for devices subjected to microwave powers of 210 W, 490 W, 700 W, and 980 W, focusing on the statistical data related to their electrical parameters. Our findings demonstrate an improvement in device performance that correlates with an increase in annealing power, with the peak enhancement in the on-state current occurring at 700 W. This result aligns with findings from other researchers. Other electrical performance metrics also achieved optimal levels at this power setting. Through this study, we have identified the optimal annealing power for molybdenum disulfide devices via MWA and provided guidelines for the annealing process. Additionally,

our method for thickness recognition does not rely on the material properties but solely on the optical color space, suggesting potential applicability for thickness recognition in other two-dimensional materials, thereby aiding in the preparation of large datasets for other two-dimensional devices.

Author Contributions: Conceptualization, X.S. and H.Y.; Methodology, X.S.; Software, X.S.; Validation, X.S. and Y.Z.; Formal analysis, X.S.; Investigation, S.C. and Y.Z.; Resources, D.W.; Data curation, S.C. and Y.Z.; Writing—original draft, X.S.; Writing—review & editing, X.S., S.C., Y.Z. and H.Y.; Visualization, X.S. and S.C.; Supervision, H.Y. and D.W.; Project administration, H.Y. All authors have read and agreed to the published version of the manuscript.

Funding: This research was funded by the National Natural Science Foundation of China: 62374044.

Institutional Review Board Statement: Not applicable.

Informed Consent Statement: Not applicable.

Data Availability Statement: The original contributions presented in the study are included in the article, further inquiries can be directed to the corresponding authors.

Conflicts of Interest: The authors declare no conflicts of interest.

References

1. Liu, Y.; Gu, F. A wafer-scale synthesis of monolayer MoS_2 and their field-effect transistors toward practical applications. *Nanoscale Adv.* **2021**, *3*, 2117–2138. [CrossRef]
2. Tung, R.T. Recent advances in Schottky barrier concepts. *Mater. Sci. Eng. R Rep.* **2001**, *35*, 1–138. [CrossRef]
3. Wang, J.; Yao, Q.; Huang, C.-W.; Zou, X.; Liao, L.; Chen, S.; Fan, Z.; Zhang, K.; Wu, W.; Xiao, X.; et al. High Mobility MoS_2 Transistor with Low Schottky Barrier Contact by Using Atomic Thick h-BN as a Tunneling Layer. *Adv. Mater.* **2016**, *28*, 8302–8308. [CrossRef]
4. Tong, X.; Ashalley, E.; Lin, F.; Li, H.; Wang, Z.M. Advances in MoS_2-Based Field Effect Transistors (FETs). *Nano-Micro Lett.* **2015**, *7*, 203–218. [CrossRef] [PubMed]
5. Fang, H.; Chuang, S.; Chang, T.C.; Takei, K.; Takahashi, T.; Javey, A. High-Performance Single Layered WSe_2 p-FETs with Chemically Doped Contacts. *Nano Lett.* **2012**, *12*, 3788–3792. [CrossRef] [PubMed]
6. Das, S.; Chen, H.-Y.; Penumatcha, A.V.; Appenzeller, J. High Performance Multilayer MoS_2 Transistors with Scandium Contacts. *Nano Lett.* **2013**, *13*, 100–105. [CrossRef] [PubMed]
7. Park, H.K.; Jo, J.; Hong, H.K.; Heo, J. Influence of post-deposition annealing on the electrical properties of zinc oxide thin films. *Thin Solid Films* **2014**, *573*, 22–26. [CrossRef]
8. Kwon, H.-J.; Kim, S.; Jang, J.; Grigoropoulos, C.P. Evaluation of pulsed laser annealing for flexible multilayer MoS_2 transistors. *Appl. Phys. Lett.* **2015**, *106*, 113111. [CrossRef]
9. Ohshima, T.; Yoshikawa, M.; Itoh, H.; Kojima, K.; Sohei, O.; Nashiyama, I. Influence of Post-Oxidation Annealing on Electrical Characteristics in 6H-SiC MOSFETs. *Mater. Sci. Forum* **2000**, *338–342*, 1299–1302. [CrossRef]
10. Vinogradova, G.I.; Anzina, L.V.; Menshchikova, T.K.; Fedorov, V.A. Thermal Annealing As a Means of Controlling the Properties of the Magnetic Semiconductor $CdCr_2Se_4$. *Inorg. Mater.* **2019**, *55*, 1092–1096. [CrossRef]
11. Ozaki, R.; Shinpo, T.; Moritake, H. Influence of Rapid Thermal Annealing on Molecular Orientation of Planar Cholesteric Liquid Crystal. *Mol. Cryst. Liq. Cryst.* **2009**, *510*, 116/[1250]–125/[1259]. [CrossRef]
12. Bae, H.; Jun, S.; Kim, C.-K.; Ju, B.-K.; Choi, Y.-K. Quantitative analysis of trap states through the behavior of the sulfur ions in MoS_2 FETs following high vacuum annealing. *J. Phys. D Appl. Phys.* **2018**, *51*, 105102. [CrossRef]
13. Yang, R.; Zheng, X.; Wang, Z.; Miller, C.J.; Feng, P.X.-L. Multilayer MoS_2 transistors enabled by a facile dry-transfer technique and thermal annealing. *J. Vac. Sci. Technol. B* **2014**, *32*, 061203. [CrossRef]
14. Roh, J.; Lee, J.; Jin, S.H.; Lee, C. Negligible hysteresis of molybdenum disulfide field-effect transistors through thermal annealing. *J. Inf. Disp.* **2016**, *17*, 103–108. [CrossRef]
15. Zhang, Y.; Su, X.; Cui, S.; Yang, H.; Wu, D. Enhance the Electrical and Photoelectrical Performance of MoS_2 Transistor With Polyimide Gate Dielectric by Microwave Annealing. *IEEE Trans. Electron Devices* **2024**, *71*, 2736–2741. [CrossRef]
16. Su, X.; Wu, D. Microwave Annealing for Enhanced Performance of Flexible MoS_2 FET Based on Electromagnetic Losses in Electrode. *IEEE Trans. Electron Devices* **2024**, *71*, 860–866. [CrossRef]
17. Hong, E.-K.; Cho, W.-J. Effect of microwave annealing on SOI MOSFETs: Post-metal annealing with low thermal budget. *Microelectron. Reliab.* **2017**, *80*, 306–311. [CrossRef]
18. Fu, C.; Wang, Y.; Xu, P.; Yue, L.; Sun, F.; Zhang, D.W.; Zhang, S.-L.; Luo, J.; Zhao, C.; Wu, D. Understanding the microwave annealing of silicon. *AIP Adv.* **2017**, *7*, 035214. [CrossRef]
19. Yang, H.; Li, C.; Yue, L.; Wen, C.; Zhang, J.; Wu, D. Improving electrical performance of few-layer MoS_2 FETs via microwave annealing. *IEEE Electron Device Lett.* **2019**, *40*, 1116–1119. [CrossRef]

20. Lee, Y.H.; Zhang, X.Q.; Zhang, W.; Chang, M.T.; Lin, C.T.; Chang, K.D.; Yu, Y.C.; Wang, J.T.; Chang, C.S.; Li, L.J.; et al. Synthesis of large-area MoS_2 atomic layers with chemical vapor deposition. *Adv. Mater.* **2012**, *24*, 2320–2325. [CrossRef]
21. Bergeron, H.; Sangwan, V.K.; McMorrow, J.J.; Campbell, G.P.; Balla, I.; Liu, X.; Bedzyk, M.J.; Marks, T.J.; Hersam, M.C. Chemical vapor deposition of monolayer MoS_2 directly on ultrathin Al_2O_3 for low-power electronics. *Appl. Phys. Lett.* **2017**, *110*, 053101. [CrossRef]
22. Zhang, W.; Chiu, M.H.; Chen, C.H.; Chen, W.; Li, L.J.; Wee, A.T. Role of metal contacts in high-performance phototransistors based on WSe_2 monolayers. *ACS Nano* **2014**, *8*, 8653–8661. [CrossRef] [PubMed]
23. Yu, Y.; Li, C.; Liu, Y.; Su, L.; Zhang, Y.; Cao, L. Controlled scalable synthesis of uniform, high-quality monolayer and few-layer MoS_2 films. *Sci. Rep.* **2013**, *3*, 1866. [CrossRef] [PubMed]
24. Lee, C.; Yan, H.; Brus, L.E.; Heinz, T.F.; Hone, J.; Ryu, S. Anomalous lattice vibrations of single- and few-layer MoS_2. *ACS Nano* **2010**, *4*, 2695–2700. [CrossRef] [PubMed]
25. Liby, J.; Jaya, T. HSV model based data hiding in video for watermark applications. *J. Intell. Fuzzy Syst.* **2021**, *41*, 2731–2742. [CrossRef]
26. Flores-Vidal, P.; Gómez, D.; Castro, J.; Montero, J. New Aggregation Approaches with HSV to Color Edge Detection. *Int. J. Comput. Intell. Syst.* **2022**, *15*, 78. [CrossRef]
27. Jiang, X.; Pang, Y.; Li, X.; Pan, J.; Xie, Y. Deep neural networks with Elastic Rectified Linear Units for object recognition. *Neurocomputing* **2018**, *275*, 1132–1139. [CrossRef]
28. Kingma, D.P.; Ba, J. Adam: A method for stochastic optimization. *arXiv* **2014**, arXiv:1412.6980. [CrossRef]
29. Ruder, S. An overview of gradient descent optimization algorithms. *arXiv* **2016**, arXiv:1609.04747. [CrossRef]
30. Sirota, B.; Glavin, N.; Voevodin, A.A. Room temperature magnetron sputtering and laser annealing of ultrathin MoS_2 for flexible transistors. *Vacuum* **2019**, *160*, 133–138. [CrossRef]
31. Jin, H.; Xing, Z.; Yangyuan, W.; Ru, H. New method for extraction of MOSFET parameters. *IEEE Electron Device Lett.* **2001**, *22*, 597–599. [CrossRef]

Disclaimer/Publisher's Note: The statements, opinions and data contained in all publications are solely those of the individual author(s) and contributor(s) and not of MDPI and/or the editor(s). MDPI and/or the editor(s) disclaim responsibility for any injury to people or property resulting from any ideas, methods, instructions or products referred to in the content.